A Measurement of the Angular Power Spectrum of the Anisotropy in the Cosmic Microwave Background

C. B. Netterfield, M. J. Devlin, N. Jarosik, L. Page and E. J. Wollack[1]

Princeton University, Department of Physics, Jadwin Hall,
Princeton, NJ, 08544

ABSTRACT

We report on a measurement of the angular power spectrum of the anisotropy in the Cosmic Microwave Background. The anisotropy is measured in 23 different multipole bands from $\ell = 54$ ($\approx 3°$) to $\ell = 404$ ($\approx 0.45°$) and in 6 frequency bands from $26\,\mathrm{GHz}$ to $46\,\mathrm{GHz}$ over three observing seasons. The measurements are consistent from year to year. The frequency spectral index of the fluctuations (measured at low ℓ) is consistent with that of the CMB and inconsistent with either dust or Galactic free-free emission. Furthermore, the observations of the MSAM1-92 experiment (Cheng et al. 1994) are repeated and confirmed. The angular spectrum shows a distinct rise from $\delta T_\ell \equiv \sqrt{\ell(2\ell+1) < |a_\ell^m|^2 > /4\pi} = 49^{+8}_{-5}\,\mu\mathrm{K}$ at $\ell = 87$ to $\delta T_\ell = 85^{+10}_{-8}\,\mu\mathrm{K}$ at $\ell = 237$. These values do not include an overall $\pm 14\%$ (1σ) calibration uncertainty. The analysis and possible systematic errors are discussed.

Subject headings: cosmic microwave background — cosmology: observations

---

[1]NRAO, 2015 Ivy Rd., Charlottesville, VA, 22903

1. Introduction

The discovery of the anisotropy in the cosmic microwave background (CMB) by the COBE satellite (Smoot et al. 1992; Bennet et al. 1992) and its subsequent confirmation (Ganga et al. 1993) at large angular scales (greater than 7°) has been followed by positive detections of anisotropies in the microwave sky at intermediate angular scales by a number of other experiments (De Benardis et al. 1994; Devlin et al. 1994; Dragovan et al. 1994; Gundersen et al. 1995; Gutierrez et al. 1995) and upper limits at smaller angular scales (Meyers, Readhead, & Lawrence 1993; Tucker et al. 1993). In order to reject foreground contamination, most of these experiments observe the sky over a range of frequencies. Additionally, several have successfully repeated their measurements of previous years.

Characterization of the anisotropy at medium angular scales (2° to 0.2°) can strongly constrain theories of structure formation and cosmological parameters, mainly through the angular power spectrum of the anisotropy (Bond et al. 1994; Crittenden & Turok 1995; Kamionkowski et al. 1994; Jungman et al. 1995. For a recent review of the CMB see White, Scott, & Silk 1994).

We present results from an experiment designed to measure the angular power spectrum of the CBR at medium angular scales. The SK telescope observes from the ground in Saskatoon, Saskatchewan, Canada. The observing scheme has many internal consistency tests which allow checks of the integrity of the measurement. A frequency span of $20\,\mathrm{GHz}$ provides discrimination against foreground contaminants. Measurements made by this experiment are consistent from year to year. In addition, we have reproduced the results of the MSAM1-92 (Cheng et al. 1994) experiment. Partial descriptions of the SK instrument are given in Wollack et al. 1993 (SK93), Wollack 1994 (SK93), Wollack et al. 1994, Page et al. 1994, Netterfield 1995 (SK94) and Netterfield et al. 1995 (SK93 to SK94 comparison). The instrument and calibration is described in detail in Wollack et al. 1996. Previous results (SK93 and SK94) are included in this analysis.

2. Instrument and Calibration

The SK telescope is comprised of a corrugated feed horn illuminating a parabolic primary followed by a chopping flat with a vertical chopping axis. The telescope is steerable in azimuth, but fixed in elevation. Observations are made in $\mathrm{K_a}$-band (26 GHz to 36 GHz) and Q-band (36 GHz to 46 GHz). Observations made in each band are broken up into 3 frequency sub-bands and two linear polarizations. Total power radiometers based on HEMT amplifiers are used. The supernova remnant Cas-A is used to calibrate the telescope and determine the beam size and pointing. Table 1 lists the beam parameters and uncertainties. The beam widths are known to better than 2%. The calibration uncertainty is comprised of a 13% contribution due to uncertainty in the absolute calibration of Cas-A, which is constant between years and radiometers, and a 3% to 5% contribution due to measurement uncertainty.

The telescope pointing is determined from the position of Cas-A. In 1995, the telescope was pointed 0.05° differently than was intended, which was included in the analysis. In 1994, the discrepancy was less than 1/10 of a beam, and was ignored. In addition, there was a $0.03°$ (1σ) jitter in the beam position from the chopping plate and base pointing accuracy. When convolved with the beam, this can be approximated by adding this uncertainty in quadrature to the nominal beam width. For 1995 this is results in a 1% widening of the effective azimuth beam.

3. Observing Strategy: Synthesized Beams

The observing strategy is designed to offer a variety of internal systematic checks, minimize contamination by atmospheric temperature gradients, and to simultaneously probe a variety of angular scales. These goals are achieved by sweeping the beam in azimuth on the sky by many beam widths with a large chopping flat, and then synthesizing effective antenna patterns in software. For simplicity in the discussion which follows, telescope and observing parameters for the 1995 season are used. Parameters for all years are listed in Table 1.

As the beam is swept on the sky, the radiometer is sampled 168 times per complete sweep. In analysis the 168 samples from each sweep, T_i, are multiplied by a weighting vector, w_i, to give $\Delta T_{sweep} = \sum w_i T_i$. By choice of weighting vector the relative weighting of each spatial point in the sweep can be set allowing the synthesis of arbitrary effective antenna sensitivity

TABLE 1

OBSERVING PARAMETERS

		K_a93	K_a94	Q94	Q95 Cap	Q95 RING
Beam	x FWHM	$1.42 \pm 0.005°$	$1.42 \pm 0.005°$	$1.004 \pm 0.005°$	$0.461 \pm 0.003°$	$0.461 \pm 0.003°$
	y FWHM	$1.42 \pm 0.02°$	$1.42 \pm 0.02°$	$1.08 \pm 0.02°$	$0.513 \pm 0.004°$	$0.513 \pm 0.004°$
Chopper	Pattern	Sine	Linear	Linear	Sine	Sine
	Amplitude on Sky	$4.90°$	$7.00°$	$7.35°$	$7.96°$	$3.36°$
	Rate	3.906 Hz	3.906 Hz	3.906 Hz	2.976 Hz	2.976 Hz
	Samples/Sweep	16	64	64	168	168
Pointing	Azimuth (W:E)	$-8.2° : 7.8°$	$-7.15° : 7.25°$	$-7.15° : 7.25°$	$-7.392° : 7.288°$	$0.14°$
	Jitter	$\ldots$	$0.02°$	$0.02°$	$0.03°$	$0.03°$
	Elevation	$52.2°$	$52.2°$	$52.2°$	$52.24°$	$60.2°$
Timing	Time Per Base Move	16.4 s	20 s	20 s	40.3 s	2 weeks
	File Length	17 min	15 min	15 min	20 min	20 min

patterns, $H(x, y)$, given by

$$H(\mathbf{x}) = \left\langle \sum_i w_i G(\mathbf{x} - \mathbf{X}_i) \right\rangle_{bin} \qquad (1)$$

where $\mathbf{X}_i$ is the position on the sky of the center of the main beam corresponding to weighting vector element w_i and

$$G(x, y) = \frac{1}{2\pi\sigma_x\sigma_y} \exp\left(-\frac{x^2}{2\sigma_x^2} - \frac{y^2}{2\sigma_y^2}\right) \qquad (2)$$

is the main beam pattern of the telescope pointed at $(0, 0)$. The azimuth dimension is denoted by x and the elevation dimension by y. The beam width of the telescope is given by $\sigma = FWHM/\sqrt{8\ln(2)}$. The effect of the rotation of the Earth during an integration is included in $H(\mathbf{x})$, as denoted by $< \ldots >_{bin}$.

For example, if the weighting vector w_i is selected so that data which are acquired when the chopping plate is centered are given a positive weight, and data which are acquired when the chopping plate is offset to the left or right are given negative weight, then a three lobed synthesized beam on the sky is produced (hereafter referred to as the 3pt synthesized beam). The weighting vectors are normalized so that $\int |H(\mathbf{x})|d\mathbf{x} = 2$ for a single sweep, not including the rotation of the Earth. The mean of the weighting vector is zero in order to eliminate sensitivity to fluctuations in the mean temperature of the sky. Since

the weighting vectors for different effective antenna patterns are made to be nearly orthogonal all of the effective antenna patterns may be acquired from the same data. Synthesized antenna patterns up to 19pt (≈ 60 Hz) are produced. The number of lobes is limited by the beam size to throw ratio, and not by the detectors.

The synthesis of the 9pt beams is demonstrated in Figure 1. Figure 2 displays some of the synthesized beams. In total, including the three years, there are 37. The 3pt through 9pt antenna patterns are similar for K_a94, Q94 and Q95, allowing these data to be compared. Since the sweep amplitude and pointing for SK93 was substantially different than for the other years, the K_a93 3pt beam is also substantially different. Comparing SK93 with SK94 requires the use of a specially optimized weighting vector (K_a93 overlap).

Data are acquired in two modes: In the first mode (*Cap* Data), which was used all three years, the chopping plate axis is vertical which places the beam at a constant elevation of $52.2°$, the elevation of the North Celestial Pole (NCP) in Saskatoon. The beam is swept sinusoidally $12.8°$ in azimuth ($7.35°$ peak to peak on the sky) at 2.976 Hz. The center of the sweep is alternated every 40.3 seconds between $7.32°$ East of the NCP and $7.28°$ West of the NCP. As the earth rotates throughout the day, the celestial polar cap is covered, from the NCP to $82°$ declination. Data ac-
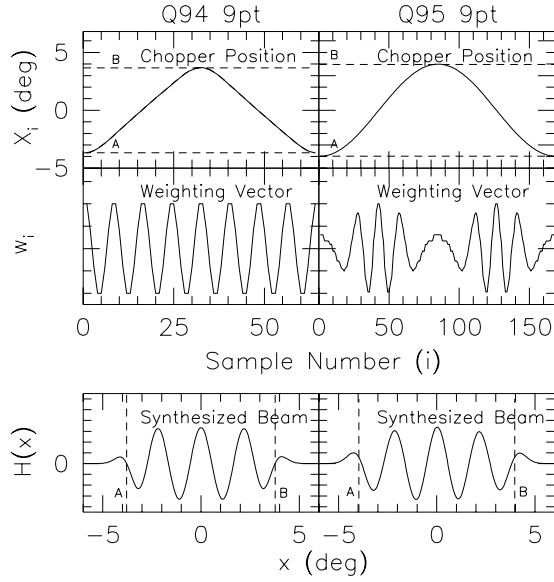
Fig. 1.— Beam Synthesis. Shown is the synthesis of the 9pt beams for Q94 and Q95 using equation (1). $H(x)$ is shown along the path of the swept beam. The effect of binning in RA is neglected here for clarity. In 1994, an approximately linear sweep pattern, $\mathbf{X}_i$, was used as shown. This allowed the use of sinusoidal weighting vectors, w_i, to produce synthesized beams with equally spaced lobes. The use of a sinusoidal sweep rendered this impossible in 1995. The Q95 weighting vectors were generated by optimizing the sensitivity of the synthesized beam to a specified band of angular scales. Spatially similar synthesized beams are produced.
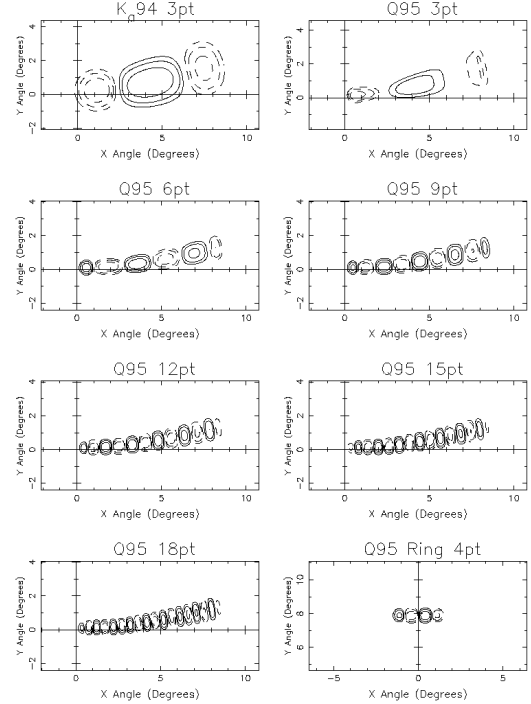
Fig. 2.— Synthesized Beams. The contour lines are every 3dB. Dashed lines denote negative weighting. The NCP is located at (0,0). Straight lines from the NCP are lines of constant hour angle. The bottom right plot is of the *Ring* 4pt synthesized beam, which is centered 8° above the NCP. The remaining plots are of *Cap* data acquired in the East. The curvature is due to the fact that the beam is swept in azimuth, and not declination. The lobes farthest from the NCP are wider in RA than those closest because the data are averaged into 24 (3pt to 5pt) or 48 RA bins.

quired in the East are repeated ≈ 12 hours later in the West, giving a very powerful systematic test. These data are multiplied by weighting vectors which produce a family of synthesized beams on the sky from 3pt to 19pt, and are then integrated into 24 (for 3pt to 5pt) or 48 (for 6pt to 19pt) bins in Right Ascension (RA).

In the second mode (*Ring* Data), which was only used in 1995, the chopping plate is tilted back 4.0° which raises the beam elevation 8.0° to 60.2°. The telescope is pointed so that the center of the sweep is North. The beam is swept sinusoidally with a peak to peak amplitude of 3.36°on the sky. In the small angle approximation, the beam is swept in RA at a constant declination. As the Earth rotates an entire ring at 82° declination is sampled.

Synthesized beams are generated in the same way as with the *Cap* data, except that a new weighting vector must be generated every sweep to keep the synthesized beam fixed in RA during its integration. The synthesized beams are smaller than the amplitude of the sweep which allows positions on the sky to be tracked in software. Three point to 6pt synthesized beams are produced, as well as the effective 3pt beam pattern of the MSAM1-92 experiment. The *Ring* data lacks the East to West comparison test of the *Cap* data. However, synthesis of the MSAM beam makes it possible to compare directly with a very different experiment.

4.   Data Selection and Reduction

Because the SK telescope observes from the ground in Saskatoon, an important part of the analysis is the selection of data where contamination from atmospheric spatial temperature fluctuations do not dominate. The first cut is made by evaluating, for each 20 minute file, the mean deviation of 8 second averages made with a beam synthesized using a 2pt weighting vector which is sensitive to the horizontal component of spatial temperature gradients. This number is large when the spatial gradient is changing and small when it is stable and has been found to be a good indicator of atmospheric contamination. The mean deviation is used because it is less sensitive than the standard deviation to spikes in the data, which are more likely to be due to birds or airplanes than to atmospheric noise. The mean deviation is related to the standard deviation by $\Delta_x = \sqrt{\frac{2}{\pi}}\sigma_x$ for normal distributions.

A more general expression for the cut levels is given
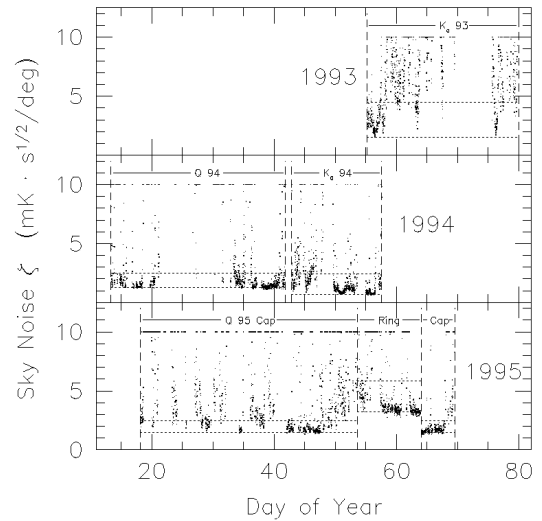
Fig. 3.— The sky noise in Saskatoon. The value ζ is a measure of the stability of the horizontal component of spatial temperature gradients (see text). The upper dashed line in each plot denotes the nominal atmospheric cut. The lower dashed line indicates the system noise limit, $\zeta_n = \kappa \mathrm{NET}/\theta_{eff}$. The noise floor for the 1995 *Ring* data is higher than for the *Cap* data because θ_{eff} is smaller. Data with $\zeta > 10$ mK· s$^{1/2}$/ deg have been limited to $\zeta = 10$ mK· s$^{1/2}$/ deg in this plot. The maximum value of ζ recorded was 1360 mK· s$^{1/2}$/ deg.

by
$$\zeta = \sigma\sqrt{\tau}/\theta_{eff} \qquad (3)$$
where σ is the standard deviation of the 2pt data, τ is the integration time, and
$$\theta_{eff} = \int \theta_x H(\theta_x, \theta_y) d\theta_x d\theta_y \qquad (4)$$
is the effective sweep amplitude in degrees. The units of ζ are $mK \cdot s^{1/2}/\deg$. Neglecting the radiometer contribution, this measurement of the stability of the atmosphere may be compared from experiment to experiment. The effective sky noise, ζ_n, due to the receiver NET is given by $\zeta_n \equiv \kappa\text{NET}/\theta_{eff}$, where $\kappa = \sqrt{N\sum_i w_i^2}$, and N is the number of samples per sweep.

Figure 3 shows ζ as a function of time for each of the observing seasons. Horizontal dashed lines are the nominal cut levels (the upper line) and the receiver noise level, ζ_n (the lower line), for each of the observing runs. Each point represents the result for one file of data (see Table 1). Because the throw for the *Ring* data was significantly smaller than for the *Cap* data, ζ_n is significantly higher. In other words, the *Ring* observations are significantly less sensitive to the atmospheric gradients than the *Cap* observations.

It is furthermore required that for a file to be accepted, the files before and after must also pass the atmospheric cuts. Thus, the sky must be stable for three files (45 minutes in 1994 and 60 minutes for 1995) for any data to be accepted at all. Of the data acquired, 27% passes the nominal cut. Table 2 summarizes the amount of data acquired in each observing mode at different cut levels. The cut level listed first for each experiment is the one used for the definitive data set. The lower cut data for the *Ring* is comprised of the two long receiver noise limited stretches around day 59 and day 63 of 1995 rather than being based on specific sky noise level. The analysis is performed for each of the listed cut levels (see Table 11). Decreasing the cut level from the definitive values changes the spectrum by approximately 1σ for the SK95 data. Because this lower cut level is so close to the receiver noise, good data are cut at random, reducing the length of contiguous stretches of data. This increases sensitivity to long time scale noise and reduces the robustness of error bar calculation. Increasing the cut level has an insignificant effect on the results.

The data are blanked for base moves (e.g. 4 seconds every 40 seconds for SK95) and for spikes which

may be due to birds, planes or occasional glitches in the data system. An entire sweep of data is blanked if any of the samples in it (64 for SK94, and 168 for SK95) exceed the mean by more than some limit (3.5σ for SK94 and 3.85σ for SK95). The amount of data removed in this step is consistent with the data being normally distributed (15% for SK95).

The data are then multiplied by the weighting vector and binned according to RA. A weighted mean of the frequency and polarization channels is also made before application of the weighting vector for analyses where frequency and polarization information are not required. For the *Ring* data, a new weighting vector is generated every sweep so that the antenna pattern in each bin is fixed in RA, while for the *Cap* data, the weighting vectors are fixed. The *Cap* data acquired in the East are binned separately from the data acquired in the West. The bin numbering for both East and West data is based on the RA of the center of the sweep when the telescope is pointed in the East.

For the *Cap* data, the error bars are generated in two stages. First, after beam synthesis, the data are averaged into bins 15 sidereal minutes wide. Weights for each bin are calculated based on the distribution of 18 second averages. If any 18 second average is more than 3.5σ away from the mean of the bin it is cut. These 15 min averages are then binned into 24 or 48 bins around the sky with weights propagated from the weights of the 15 minute averages. These weights are used to give the relative weighting of each RA bin. The overall weighting is generated from the distribution of the 15 minute bins after removal of corresponding mean signal from the 24 or 48 RA bins. For data weighted to synthesize many lobed beams (6pt or more) the error bars based on 18 second averages agree to 10% with those based on 15 minute averages, but for the 3pt or 4pt data (which is more sensitive to atmospheric noise) the distribution of 15 minute averages predicts error bars as much as 50% larger than would be generated from the distribution of the 18 second averages (see Table 3). For the *Ring* data, with its substantially smaller sweep which yields much less sensitivity to the atmosphere, the error bars are generated directly from the distribution of the 18 second averages.

5. Offsets

The design of the SK telescope is intended to minimize the instrumental offset. However, the emis-

sion from the large chopping plate is a function of the plate orientation, which theoretically produces a $\approx -400\,\mu\mathrm{K}$ offset for the horizontally polarized channel and a $\approx 200\,\mu\mathrm{K}$ offset in the vertically polarized channel in the 3pt data. The measured 3pt offsets are approximately this magnitude for SK93 and SK94. In SK95, however, an additional $\approx -1\,\mathrm{mK}$ offset was present in both polarizations. The source of this additional offset is not known. See Wollack et al. 1996 for possible explanations.

The offsets are dealt with differently between the *Cap* and *Ring* data analysis. In the *Cap* analysis, the weighting w_i is constant for a given synthesized beam and chopping plate orientation. For this reason the offsets are ignored until the data have been multiplied by the weighting vector and binned in RA. At that point, the mean value of the 24 or 48 RA bins is removed. The error bars are then multiplied by $\sqrt{24/23}$ or $\sqrt{48/47}$ to compensate for the removed degree of freedom. The levels of the *Cap* offsets for each synthesized beam are listed in Table 3.

For the *Ring* data, however, a new weighting vector must be calculated for each sweep, which causes the offset to change as the synthesized beam is tracked over the sky. To deal with this, all of the accepted data are coadded synchronously with the sweep to form a 168 sample mean sweep. This mean sweep, which is essentially the instrumental offset as a function of chopping plate position, is subtracted from the data for each sweep prior to multiplication by the weighting vector. At this point then, the offset for any synthesized *Ring* beam is zero.

As evidenced by the larger in scatter of the 15 minute averages compared to that predicted by the distribution of the 18 second averages in the *Cap* data (see Table 3), there may be some drift to this offset on longer time scales. Since at least some of offset is due to emission, the excess long time scale noise could be expected to correlate with the temperatures of the optical components. The correlations are not significant ($\approx 1\sigma$) however, and regressing out the optics temperatures has no effect on the long time scale noise. Since the gain of the amplifiers is a function of temperature the long time scale noise might be expected to vary with receiver temperature. But, as with the optics temperatures, there is no significant correlation with receiver temperature, and regressing it out has no effect. In the final analysis, nothing is regressed out.

To further investigate the effect of the excess long

time scale noise in the *Cap* data, polynomials in time (linear to 9th degree) were fit out of the data. The maximum slope from fitting a line in time to the data is $7\,\mu\mathrm{K}$ per day for the SK95 3pt data. The typical slope is less than $1\,\mu\mathrm{K}$ per day and consistent with zero. As with regressing out the auxiliary temperatures, removing lines or polynomials has no significant effect on the long time scale noise or on the final angular power spectrum. In the final analysis, only the constant offset is removed.

To test the possibility that the long time scale noise is due to instrumental drifts, data taken in the West can be subtracted from data taken in the East 40 seconds earlier. Doing this decreases the differences between the short and long time-scale based error bars. This subtraction, however, has no significant effect on the spectrum, beyond increasing the error bars: $(E - W)/\sqrt{2}$ will have the same *rms*, as E or W by themselves, but now there is only one data set to do statistics on, rather than two. It is also possible that the excess long time scale noise is due to atmospheric contamination: this was the interpretation taken by the OVRO Ring experiment (Readhead et al. 1989) for a similar effect.

6. Internal Consistency Checks

The observing scheme used in the SK experiment has a number of internal consistency checks. For the *Cap* data, the rotation of the Earth causes the same sky as was observed with the telescope pointed to the East of the NCP to be observed ≈ 12 hours later when the telescope is pointed to the West. This test $(E - W)$ gives assurance that the signal which has been observed is truly on the sky: contamination from the atmosphere or ground pickup could be expected to repeat on a 24 solar hour time scale, not a 24 sidereal hour time scale with the signal in the East lagged 12 sidereal hours from the signal in the West.

The data set may also be divided into first half ($H1$) and second half ($H2$), and compared. Since there is approximately one month between the centroids of the first and second half, the success of this test gives assurances that the observed signal repeats on sidereal time, and not solar time: if the signal repeated on solar time, the signal between halves would be lagged by 4 out of 48 bins. This places limits on contamination by the sun and any Radio Frequency Interference (RFI) that recurs daily.

The data from the two polarization channels (A

TABLE 4
INTERNAL CONSISTENCY TESTS I: 3PT TO 9PT *Cap*

	K$_a$93 Overlap	3pt	4pt	5pt	6pt	7pt	8pt	9pt
K$_a$93 Sum	3.76	...	...	...	...	...	...	...
E−W	1.17	...	...	...	...	...	...	...
A−B	1.0	...	...	...	...	...	...	...
K$_a$94 Sum	5.20	4.59	2.16	2.92	1.47	1.40	1.13	1.03
A−B	0.79	0.55	0.67	0.70	0.85	0.94	0.88	1.18
E−W	0.76	0.88	0.83	0.70	1.17	1.06	1.39	0.59
Quadrature	...	1.2	0.7	1.0	1.2	1.3	...	...
Q94 Sum	3.21	2.15	1.97	1.14	1.06	1.27	1.19	1.53
E−W	0.91	0.67	1.06	1.09	0.68	1.08	1.05	0.84
Quadrature	...	0.7	1.1	1.0	1.1	1.4	...	...
Q95 Sum	...	2.64	1.98	3.27	2.49	2.49	2.69	2.37
A−B	...	0.91	1.05	1.09	0.74	0.73	1.1	1.0
E−W	...	1.13	0.99	1.22	1.12	1.60	1.09	1.16
H1−H2	...	2.34	1.60	1.05	1.13	1.09	1.06	0.88
Quadrature	...	0.93	1.23	1.37	1.49	0.90	1.21	0.99
K$_a$93+K$_a$94	6.12	...	...	...	...	...	...	...
K$_a$93−K$_a$94	1.18	...	...	...	...	...	...	...
K$_a$94+Q94	7.17	6.01	2.91	3.35	1.66	1.52	1.50	1.58
K$_a$94−Q94	1.25	0.73	1.22	0.71	0.87	1.15	0.82	1.03
K$_a$94+Q95	...	6.01	2.94	5.21	2.53	2.50	2.66	2.56
K$_a$94−Q95	...	1.22	1.20	0.98	1.43	1.29	1.17	0.85
Q94+Q95	...	4.10	2.85	2.92	2.07	2.69	3.10	2.94
Q94−Q95	...	0.69	1.09	1.49	1.48	1.06	0.78	1.02

NOTE.— Reduced χ^2 for a variety of internal symmetry tests for 3pt to 9pt data. The *Sum* entries indicate the reduced χ^2 for the total signal on the sky (with A and B polarizations averaged and data acquired in the East and in the West averaged). The $E − W$ entries indicate the residual signal if data acquired in the West is subtracted from data acquired in the East 12 hours earlier. The $A − B$ entries represent the residual if the two polarizations are differenced. The *Quadrature* entries give the amplitude of the signal if the weighting vector is modified to have no sensitivity on the sky. The K$_a$*93 Overlap*, 3*pt*, 4*pt* and 5*pt* entries have 23 degrees of freedom. The rest have 47 degrees of freedom. The *Sum* entries have consistently larger reduced χ^2 entries than the the control entries, indicating the presence of a true sky signal.

TABLE 5
INTERNAL CONSISTENCY TESTS II: 10PT TO 19PT *Cap*

	10pt	11pt	12pt	13pt	14pt	15pt	16pt	17pt	18pt	19pt
Q95 Sum	1.95	2.12	2.29	2.30	1.71	1.94	1.62	1.70	1.51	1.18
A−B	1.01	1.36	0.78	0.85	1.36	0.96	0.88	1.04	1.17	0.97
E−W	0.85	0.81	1.29	1.42	0.90	0.85	1.21	1.21	1.01	1.36
H1−H2	0.91	1.01	1.29	0.91	1.53	1.62	0.73	1.29	1.19	1.57
Quadrature	0.97	0.90	1.22	1.05	1.30	1.31	0.81	1.14	1.09	1.26

NOTE.— Reduced χ^2 for a variety of internal symmetry tests for 10pt to 19pt SK95 *Cap* data. All entries have 47 degrees of freedom.

TABLE 6
INTERNAL CONSISTENCY TESTS III: *Ring*

	3pt	4pt	5pt	6pt	MSAM Overlap
Q95 Sum	1.86	1.83	1.34	1.01	1.87
A−B	1.16	1.31	1.40	1.28	1.55
H1−H2	1.19	1.07	1.24	1.2	1.05
Q95+MSAM1-92	· · ·	· · ·	· · ·	· · ·	3.43
Q95−MSAM1-92	· · ·	· · ·	· · ·	· · ·	1.05

NOTE.— Reduced χ^2 for a variety of internal symmetry tests for SK95 *Ring* data. The 3*pt* to 6*pt* entries have 95 degrees of freedom. The *MSAM Overlap* entries have 80 degrees of freedom.

is vertical and B is horizontal) may also be compared. This test is useful for detecting contaminants which effect the two receiver chains differently, such as data system pickup or polarized diffraction off of the ground screen.

Since the same region of sky has been observed in 1994 as 1995, the 3pt to 9pt *Cap* data can also be compared between years. A comparison of the SK93 and SK94 data using a specially prepared weighting vector for SK94 is presented in Netterfield et al. (1995) and repeated here. Since many elements of the telescope, radiometer, and ground shield were changed between years, this test can give assurances that the data have not been contaminated by side lobes, vibrations or atmospheric gradients.

Finally, weighting vectors may be applied which have the same frequency as sky-sensitive weighting vectors, but with the phase adjusted to have no sensitivity to the sky (quadrature phase). This test is sensitive to synchronous vibrational or electrical signals, which would not necessarily have the same phase as a true sky signal.

The results of this set of internal consistency tests are given in Tables 4-6. The expected reduced χ^2 for the difference tests should be distributed around 1.0 with a standard deviation of $1/\sqrt{2\nu}$, where ν is the number of degrees of freedom, assuming that the sky signals are 100% correlated and the error bars are completely uncorrelated. This is the case for the $H1 - H2$ tests, but not for the $E - W$ tests, the $A - B$ tests, or the year to year tests. The small beam, large throw in azimuth (rather than declination) and slight asymmetry in the East to West pointing of the SK95 experiment means that the $E - W$ lagged correlation is not 100%. For the 12pt data, for instance, the theoretical $E - W$ correlation coefficient (see Section 7) is $\rho_T^{EW} \equiv C_T^{EW}/\sqrt{C_T^{EE}C_T^{WW}} = 0.75$. For the 3pt data, $\rho_T^{EW} = 0.90$. In this case, where the sky signal is not 100% correlated, we find[2],

$$\chi_{E-W}^2/\nu = \frac{2\rho + (1-\rho)\chi_{E+W}^2/\nu}{1+\rho} \qquad (5)$$

---

[2]For two correlated zero mean normal deviates $\{\mathbf{x}\}$ and $\{\mathbf{y}\}$ with $\sigma_x^2 = \sigma_y^2$, we write $y_i = a_i + \rho x_i$ where $\{\mathbf{a}\}$ is uncorrelated with $\{\mathbf{x}\}$ and ρ is the correlation coefficient between $\{\mathbf{x}\}$ and $\{\mathbf{y}\}$. One finds that $\sigma_{x+y}^2 = (1+\rho)\sigma_x^2$ and $\sigma_{x-y}^2 = (1-\rho)\sigma_x^2$. After identifying $\{\mathbf{x}\}$ with the East data and $\{\mathbf{y}\}$ with the West data, and noting that $\chi^2/\nu = 1 + \sigma_{x\pm y}^2/\sigma^2$ (where σ is the instrument noise), we find equation (5).

For the 12pt data, this results in $\chi_{E-W}^2/\nu = 1.19\pm0.1$ which is consistent with the value of 1.29 which was measured from the data. Similarly, atmospheric noise correlates the error bars from the A and B polarizations in the large angular scale data. In this case we expect $\chi_{A-B}^2/\nu = (1 - \rho_D^{AB})$, where $\rho_D^{AB} \equiv C_D^{AB}/\sqrt{C_D^{AA}C_D^{BB}}$ is the noise correlation coefficient.

While the majority of the entries in Tables 4 to 6 are consistent with the the signal being fixed on the sky, there are some entries which indicate trouble. The worst entry is for Q95 3pt $H1 - H2$. The value of the reduced χ^2 is 2.34, which is inconsistent with the expected value of 1.0. The $H1 - H2$ residual is dominated by long drifts ($\approx 12\,\mathrm{hr}$), which is consistent with the earlier observation that the 3pt data are especially effected by excess long time scale noise. However, the $E - W$ tests, and more significantly, the year to year tests work well for this data set, indicating that if the entire season is used the effect of the drifts is averaged out. A similar effect at a lower level is seen in the Q95 4pt data. Without the ability to compare with the other seasons we would be much less sanguine regarding the quality of the Q95 3pt and 4pt data.

Other notably inconsistent tests are the 14pt and 15pt $H1 - H2$ tests. For both of these the $E - W$ tests are consistent with a true sky signal. However, without a comparison between years, we have no explanation for this. Despite these problems there is strong evidence that the measured signal is on the sky.

7. Likelihood Analysis

In the analysis of these data, two questions are asked: 1) is the spectral index of the fluctuations consistent with that of the CMB, and 2) what is the angular power spectrum of the fluctuations. Comparison of the data with theoretical predictions may be done by comparison with the angular power spectrum. The determination of parameters (such as the amplitude of the fluctuations at various angular scales, and their spectral indices) are made using maximum likelihood tests.

The Likelihood (or the probability density of the data, assuming a theory) is defined as

$$L = \frac{exp(-\frac{1}{2}\mathbf{t}^t\mathbf{M}^{-1}\mathbf{t})}{(2\pi)^{N/2}|\mathbf{M}|^{1/2}} \qquad (6)$$

where $\mathbf{t}$ is a data set and $\mathbf{M} = \mathbf{C}_D + \mathbf{C}_T$ is a cor-

responding covariance matrix. $\mathbf{C}_D$ is the data co-variance matrix, and $\mathbf{C}_T$ is the pixel to pixel theory covariance matrix which is a function of the model parameters. The model parameters are adjusted to maximize L. For the Saskatoon analysis, the elements of the data vector t_i correspond to data taken looking at a specified RA bin on the sky, with a specified synthesized antenna pattern, in a given frequency and polarization channel.

Confidence intervals on a parameter T are found from the distribution of $L(T)$. The best value for the parameter is determined by finding T_{max} where $L(T_{max})$ is maximized. For positive definite quantities (such as the amplitude of the fluctuations) a non-zero detection is claimed when $L(0)/L(T_{max}) > 0.15$. In this case the error bars are found by finding T_- such that

$$\frac{\int_0^{T_-} L(T)dT}{\int_0^{\infty} L(T)dT} = 0.1587 \qquad (7)$$

for the lower limit, and finding T_+ so

$$\frac{\int_0^{T_+} L(T)dT}{\int_0^{\infty} L(T)dT} = 0.8413 \qquad (8)$$

for the upper limit. When $L(0)/L(T_{max}) < 0.15$, the 95% upper limit is found by finding T' such that

$$\frac{\int_0^{T'} L(T)dT}{\int_0^{\infty} L(T)dT} = 0.95. \qquad (9)$$

For non positive definite quantities (such as spectral indices) the technique is similar, except that the lower limits of the above integrals are $-\infty$ rather than 0.

The data covariance matrix, $\mathbf{C}_D$, describes the signal due to instrumental noise in the data. The diagonal matrix elements are simply the variance of the data derived from the distribution of the 15 minute averages as described in Section 4. The off-diagonal elements, summarized in Table 7, describe other instrumental correlations. For instance, the noise between frequency channels in the same radiometer chain is correlated by gain fluctuations in the HEMT amplifiers (Jarosik 1996). Similarly, atmospheric noise introduces correlations between simultaneously acquired channels. Since the weighting vectors for SK95 are not strictly orthogonal in time, there will be noise correlations between, for example, the 13pt data and the 15pt data. The noise from data acquired in the East is also correlated with the noise from data acquired in the West 20 seconds earlier.

This is related to the excess long time-scale noise discussed previously, and may be due to the atmosphere, or drifting instrumental offsets. The noise correlation coefficients are generated from the distribution of 18 second synthesized beam averages for all simultaneously acquired data. All known correlations are included in the analysis.

The theory covariance matrix, $\mathbf{C}_T$, describes the signal due to a hypothesized sky signal (Bond 1995 and references therein; Peebles 1994; White & Scott 1994). With the theoretical temperature fluctuations on the sky expressed in spherical harmonics as

$$T(\hat{\mathbf{x}}) = \sum_{\ell,m} a_\ell^m Y_\ell^m(\hat{\mathbf{x}}), \qquad (10)$$

the theory covariance matrix can be expressed as

$$C_T^{ij} = \frac{1}{4\pi} \sum_\ell (2\ell + 1) c_\ell W_\ell^{ij}, \qquad (11)$$

where $c_\ell \equiv \langle |a_\ell^m|^2 \rangle$ and

$$W_\ell^{ij} \equiv \int d\hat{\mathbf{x}}_1 \int d\hat{\mathbf{x}}_2 H_i(\hat{\mathbf{x}}_1) H_j(\hat{\mathbf{x}}_2) P_\ell(\hat{\mathbf{x}}_1 \cdot \hat{\mathbf{x}}_2) \qquad (12)$$

is the window function. $H(\hat{\mathbf{x}})$ is the effective antenna pattern from equation (1), and $P_\ell(\hat{\mathbf{x}}_1 \cdot \hat{\mathbf{x}}_2)$ are the Legendre polynomials. The window functions associated with the Saskatoon experiment are presented in Figure 4.

Rather than expressing the sky fluctuations in terms of c_ℓ, we use

$$\delta T_\ell \equiv \sqrt{\frac{\ell(2\ell + 1)}{4\pi} c_\ell}. \qquad (13)$$

In terms of δT_ℓ the theory covariance matrix becomes

$$C_T^{ij} = \sum_\ell \delta T_\ell^2 \frac{W_\ell^{ij}}{\ell}. \qquad (14)$$

So δT_ℓ^2 is the variance per logarithmic interval of the angular spectrum of the CMB.

8. The Window Function

The angular scale to which a data set is sensitive (ℓ_e) is determined from the diagonal components of the window function, W_ℓ^{ii} as follows. The expected *rms* amplitude of the fluctuations, Δ^i, predicted by a theory for data acquired with a specified beam is

TABLE 7
THE CORRELATIONS

Between	Source	Magnitude $\left(\frac{C_D^{ij}}{\sqrt{C_D^{ii}C_D^{jj}}}\right)$
Frequency Channels	HEMT correlations, Atmosphere	0.2 - 0.7
Polarization Channels	Atmosphere	0.0 - 0.3
East/West	Atmosphere, Offset drift	0.0 - 0.2
Q95 $n$pt and $(n+2)$pt	non-orthogonal weighting vectors	0.0 - 0.2

NOTE.— A summary of the noise correlations included in the analysis and their sources.

	κ/θ_{eff}	Cut Level ζ (mK $\cdot$ s$^{1/2}$/ deg)	hours
K$_a$93	0.60	4.5	130
		3.0	79
K$_a$94	0.44	2.5	140
		1.7	107
Q94	0.42	2.5	158
		1.7	98
Q95 *Cap*	0.36	2.5	174
		3.5	242
		1.9	114
Q95 *Ring*	0.86	6.8	121
		9.7	132
		By Hand	66

Table 2: Amount of data at different cut levels. The first cut level for each experiment listed is the nominal cut used. The others are used for consistency checks. κ/θ_{eff} is used to convert ζ to receiver NET (see text).
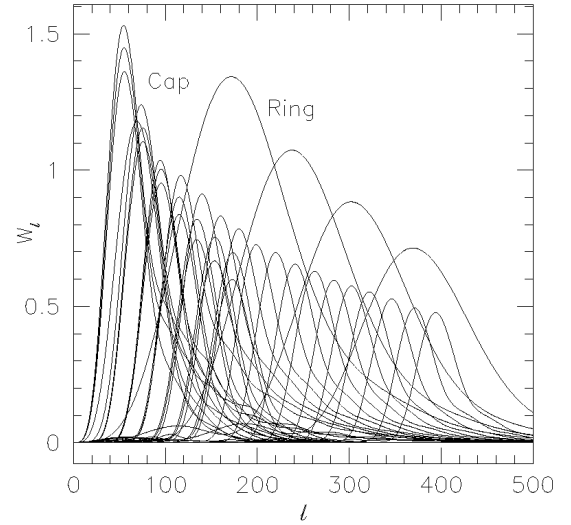

Fig. 4.— The window functions for each synthesized beam for SK93-SK95. The many-lobed *Cap* window functions are narrower than the *Ring* windows, providing finer angular resolution.

	$\dfrac{\sigma_{15min}}{\sigma_{18s}}$	A Offset	B Offset
K$_a$93 3pt	1.2	$-60 \pm 3\,\mu$K	$-360 \pm 3\,\mu$K
K$_a$94 3pt	1.1	117 ± 6	-550 ± 7
4pt	1.3	10 ± 5	-50 ± 6
5pt	1.0	54 ± 6	225 ± 6
6pt	1.0	1 ± 7	5 ± 7
7pt	1.0	7 ± 9	62 ± 9
8pt	1.0	0 ± 13	34 ± 13
9pt	1.0	80 ± 19	97 ± 18
Q94 3pt	1.2	...	-695 ± 8
4pt	1.2	...	63 ± 7
5pt	1.0	...	281 ± 8
6pt	1.0	...	15 ± 8
7pt	1.1	...	79 ± 9
8pt	1.0	...	1 ± 11
9pt	1.0	...	51 ± 13
Q95 3pt	1.5	-616 ± 13	-2182 ± 9
4pt	1.4	4 ± 11	31 ± 7
5pt	1.2	89 ± 10	436 ± 6
6pt	1.2	63 ± 9	107 ± 6
7pt	1.1	21 ± 9	145 ± 6
8pt	1.2	-56 ± 9	-83 ± 6
9pt	1.1	21 ± 9	53 ± 6
10pt	1.2	-101 ± 10	-103 ± 6
11pt	1.1	25 ± 10	35 ± 6
12pt	1.1	70 ± 10	75 ± 6
13pt	1.1	-26 ± 11	7 ± 7
14pt	1.0	-34 ± 12	-41 ± 7
15pt	1.1	-23 ± 12	-31 ± 8
16pt	1.1	-12 ± 13	-17 ± 8
17pt	1.0	15 ± 14	12 ± 9
18pt	1.1	-41 ± 15	-49 ± 9
19pt	1.0	-65 ± 17	-31 ± 10

Table 3: Offsets and long time scale noise. The ratio of error bars based on the distribution of 18s averages to error bars based on the distribution of 15 min averages is $\sigma_{15min}/\sigma_{18s}$. The 15 minute averages are used. *A Offset* is the offset in the vertically polarized channel. *B Offset* is the offset in the horizontally polarized channel. For Q94, the A receiver chain was damaged in shipping and was not used.

given by the theoretical correlation matrix (eq. [14]) as

$$\Delta^i = \sqrt{C_T^{ii}} = \sqrt{\sum_\ell \delta T_\ell^2 \frac{W_\ell^{ii}}{\ell}}, \qquad (15)$$

or the sum of the theoretical angular spectrum, weighted by W_ℓ^{ii}/ℓ. Under the assumption of a flat spectrum in δT_ℓ, this may be simplified to

$$\Delta^i = \delta T_{\ell_e} \sqrt{I(W_\ell^{ii})} \qquad (16)$$

where

$$I(W_\ell) \equiv \sum_\ell \frac{W_\ell}{\ell}. \qquad (17)$$

This provides a convenient conversion between the *rms* amplitude of the fluctuations, Δ, and the flat band power estimation, δT_{ℓ_e}. The effective ℓ for a single window function is the centroid of W_ℓ^{ii}/ℓ, or

$$\ell_e^i = \frac{I(\ell W_\ell^{ii})}{I(W_\ell^{ii})}. \qquad (18)$$

The band power estimate, $\delta T_{\ell_e}^i$, over a window function, W_ℓ^{ii}, can be generated directly from the angular spectrum, δT_ℓ, by

$$\delta T_{\ell_e^i}^2 = \frac{I(\delta T_\ell^2 W_\ell^{ii})}{I(W_\ell^{ii})}. \qquad (19)$$

When combining the results of several measurements with differing window functions it is appropriate to find the weighted mean of $\delta T_{\ell_e^i}^2$, since these are proportional to the variances, which are normally distributed far large degrees of freedom. Thus,

$$\overline{\delta T}_{\ell_e}^2 = \frac{\sum_i \delta T_{\ell_e^i}^2/\sigma_{\delta T_{\ell_e^i}^2}^2}{\sum_i 1/\sigma_{\delta T_{\ell_e^i}^2}^2} \qquad (20)$$

Inserting equation (19) into equation (20) we find

$$\overline{\delta T}_{\ell_e}^2 = \sum_\ell \delta T_\ell^2 \frac{\overline{W}_\ell}{\ell} \qquad (21)$$

where we have introduced the definition

$$\overline{W}_\ell \equiv \frac{\sum_i W_\ell^{ii}/\left(I(W_\ell^{ii})\sigma_{\delta T_{\ell_e^i}^2}^2\right)}{\sum_i 1/\sigma_{\delta T_{\ell_e^i}^2}^2}. \qquad (22)$$

$\overline{W}_\ell$ is the effective window function which results from combining band power measurements with different window functions. The quantity $\sigma_{\delta T_{\ell_e^i}^2}$ is the measurement uncertainty on $\delta T_{\ell_e^i}^2$. Note that $I\left(\overline{W}_\ell\right) \equiv 1$ with this definition.

9. The Theoretical Power Spectrum

If the angular spectrum varies slowly over the angular scales to which the experiment is sensitive it is reasonable to expand δT_ℓ as a power law in both angular scale, ℓ, and observing frequency, ν, as

$$\delta T_\ell = \delta T_{\ell_e} \left(\frac{\ell}{\ell_e}\right)^m \left(\frac{\nu}{\nu_o}\right)^\beta, \qquad (23)$$

where δT_{ℓ_e} is the amplitude of the fluctuations at angular scale ℓ_e and frequency ν_o. The angular spectral index is m and the frequency spectral index is β. With ℓ_e chosen using equation (18) and β chosen as the center frequency of the observations (i.e., 36 GHz) the three parameters are roughly orthogonal for m and β near 0. Therefore, neither the amplitude of the fluctuations, δT_ℓ, nor the frequency spectral index, β will be a function of choice of angular spectral index, m.

Determination of the frequency spectral index, β is useful for discriminating the source of the fluctuations. For the CMB $\beta = 0$, while in the Rayleigh-Jeans region for Galactic free-free emission $\beta = -2.1$, and for Galactic dust $\beta = 1.7$.

By combining data from multiple window functions the angular spectral index, m, may be determined. Since the limits on this parameter are often uninterestingly large, it is often simply set to some fixed value. Choosing $m = 0$ assumes constant δT_ℓ over the region where the data are sensitive. The determination of δT_{ℓ_e} for $m = 0$ is known as a *flat band power* estimate of the angular spectrum. The choice of $m = 1$ reproduces the "delta function" correlation function used in Wollack et al. 1993 and Netterfield et al. 1995.

The procedure for finding the angular spectrum, δT_ℓ, is to group data sensitive to a particular range of angular scales (e.g., the 5pt data are sensitive to angular scales around $\ell = 100$) and then use the maximum likelihood test to find the best amplitude, δT_{ℓ_e}, and where possible the spectral indexes, β and m, at each angular scale. Where there is insufficient leverage to determine β and m, they are fixed at 0.

Of mainly historical interest is the Gaussian autocorrelation function,

$$C_T^{ij}(\theta_{12}) = C(0) \int d\hat{\mathbf{x}}_1 \int d\hat{\mathbf{x}}_2 H_i(\hat{\mathbf{x}}_1) H_j(\hat{\mathbf{x}}_2) \exp\left(\frac{-\theta_{12}^2}{2\theta_c^2}\right), \qquad (24)$$

where $\theta_{12} = \mathrm{acos}(\hat{\mathbf{x}}_1 \cdot \hat{\mathbf{x}}_2)$. The angular spectrum associated with this is

$$\delta T_\ell = \sqrt{C(0)\frac{\ell(2\ell+1)}{2\ell_o^2}\exp\left(-\frac{\ell^2}{2\ell_o^2}\right)} \qquad (25)$$

with $\ell_o = 1/\theta_c$. The coherence angle of the theory is θ_c, and is often varied to maximize overlap with the experiment. The free parameter which is varied in a maximum likelihood test is $C(0)$. This spectrum has no particular theoretical motivation. However, since it changes only slowly over the window function of most experiments, $C(0)$ can be converted to a band power, δT_{ℓ_e} by (Bond 1995)

$$\delta T_{\ell_e} = \sqrt{C(0)\frac{I[u^2 \exp(-u^2/2)W_\ell]}{I(W_\ell)}} \qquad (26)$$

where

$$u = \frac{\ell + 1/2}{\ell_o + 1/2}. \qquad (27)$$

10. The *rms* Amplitude Analysis

It is sometimes convenient to characterize the fluctuations by their *rms* amplitude, Δ_{sky}, given by $\Delta_{sky}^2 = \Delta_{total}^2 - \Delta_{inst}^2$. The raw *rms* of the data including instrument noise is $\Delta_{total} = \sqrt{\sum \Delta T_i^2/N}$, and the estimated contribution due to instrument noise is Δ_{inst}.

The instrument noise, $\Delta_{inst} \pm \sigma_{\Delta_{inst}}$, is generated from the data covariance matrix, C_D; 4096 examples of data sets described by C_D are generated by

$$\mathbf{t} = C_D^{1/2}\mathbf{N} \qquad (28)$$

where $\mathbf{N}$ is a vector of the same dimension as $\mathbf{t}$ comprised of samples drawn from a unit normal distribution. The quantities Δ_{inst} and $\sigma_{\Delta_{inst}}$ are found from the distribution of the variances of the fake data sets. The uncertainty in Δ_{sky} due to measurement noise is given by

$$\sigma_{\Delta_{sky}}^{inst} = \frac{\Delta_{inst}}{\Delta_{sky}}\sigma_{\Delta_{inst}}. \qquad (29)$$

This determination of $\Delta_{sky} \pm \sigma_{\Delta_{sky}}^{inst}$ gives the amplitude (and uncertainty) of the fluctuations only over the region of sky which was measured, and is therefore only an estimate of the amplitude of the overall distribution from which this sample was drawn. This is appropriate for comparing different measurements of the same sky but does not include sample variance.

The uncertainty in Δ_{sky} due to sample variance $(\sigma^{SV}_{\Delta_{sky}})$ is generated from a theory covariance matrix, C_T, in the same way as $\sigma_{\Delta_{inst}}$ was generated from C_D; 4096 fake data sets described by C_T, are generated by

$$\mathbf{t} = C_T^{1/2}\mathbf{N}. \qquad (30)$$

The uncertainty $\sigma^{SV}_{\Delta_{sky}}$ is found from the distribution of the variances of the fake data sets. This estimate of the uncertainty due to sample variance is larger than what is found by a Likelihood analysis; the latter includes the effect of spatial phase information inherent in the model which the former does not (Knox 1995). The uncertainties $\sigma^{SV}_{\Delta_{sky}}$ and $\sigma^{inst}_{\Delta_{sky}}$ are added in quadrature to estimate the total uncertainty in Δ_{sky}. The *rms* amplitude, Δ_{sky}, and its uncertainties may be converted to δT_ℓ using equation (16).

11. Determination of The Frequency Spectral Index β

The first issue addressed in the analysis is whether the signal is due to the CMB or is due to some other foreground contaminant. As noted, the spectral index of most foregrounds is expected to deviate from that of the CMB, $\beta = 0$. Since data are acquired in 6 frequency bins between 26 GHz and 46 GHz, β for the fluctuations may be evaluated using the likelihood analysis described. Since the data acquired with the K_a-band radiometer only has adequate sensitivity for the 3pt, 4pt, and 5pt synthesis, this may only be done internally for angular scales below $\ell \approx 100$. The frequency span given by the Q-band data alone is inadequate to determine β.

To evaluate β the data from K_a93 3pt and SK94 & SK95 3pt to 5pt are used. The covariance matrix, $\mathbf{M}$ in equation (6) has dimension[3] 1422×1422. For the theoretical spectrum (eq. [23]) is used with $m = 0$. The likelihood analysis yields $\delta T_{\ell_e} = 47^{+7}_{-5}\,\mu\mathrm{K}$ and $\beta = 0.2^{+0.3}_{-0.3}$ for $\ell_e = 73$. Repeating the analysis with $m = -1$ yields $\beta = 0.2^{+0.3}_{-0.3}$, and $m = +1$ yields $\beta = 0.1^{+0.3}_{-0.3}$. Thus the limits on β are independent of choice of angular spectral index, m. The channel to channel calibration uncertainty is 2% to 5%. This causes an additional uncertainty in β of ± 0.1, which is to be added in quadrature to the quoted errors.

The spectral index, β, of the fluctuations is consistent with that of the CMB ($\beta = 0$), and inconsistent with known potential foreground contaminants. In particular, contamination by Galactic synchrotron ($\beta = -2.8$), Galactic free-free emission ($\beta = -2.0$) and Galactic dust ($\beta = 1.7$) in this data set are ruled out at large angular scales. Foregrounds are discussed in detail in Section 14.

12. Comparison With MSAM1-92

Perhaps the most powerful systematic check available with the Saskatoon experiment is the comparison with the MSAM1-92 experiment. MSAM1-92 is a balloon born experiment which observed the sky with a 3pt beam at a declination of 82° in ≈ 81 fields between 14.4 hr and 20.4 hr RA (Cheng et al. 1994). While the Saskatoon experiment observes the sky between 26 GHz and 46 GHz, the MSAM1-92 experiment has observing bands sensitive to the CMB at 180 GHz and 240 GHz, providing very wide frequency coverage between the two experiments. The comparison of the two experiments of very different nature places stringent limits on systematic errors or foreground contamination.

As mentioned in Section 3, data from 1995 which was acquired in the *Ring* mode (at a declination of 82.05°) was multiplied by a weighting vector which closely synthesized the MSAM 3pt beam. To generate this weighting vector, the elements w_i are adjusted to minimize the variance between the synthesized SK and MSAM beam patterns, assuming that the declination of the two experiments is equal. In reality, the mean pointing of the two experiments differs by 0.14°, and the MSAM1-92 experiment did not track in fixed elevation. This discrepancy is ignored in the in the analysis of Δ, but included in the Likelihood analysis. Once a SK weighting vector has been produced which maximizes spatial overlap, it is scaled so that $\sqrt{I(W)} = 1.15$, the value for the MSAM window function. To check the level of overlap between the the two experiments, the window function of the difference of the synthesized beams is formed. For the difference beam $\sqrt{I(W)} = 0.25$. Given this overlap, it is expected that over 90% of the sky signal will be in common between the two experiments. The window functions for the MSAM overlap are given in Figure 5.

Given the high degree of overlap expected, a naive test is adequate to verify that the two experiments see the same signal. Figure 6 shows the two data

---

[3] K_a93 has 3 frequency channels, 21 RA bins, and both East and West data (126 rows), K_a94, Q94 and Q95 each have 3 frequency channels, 24 RA bins, and East and West data for 3pt, 4pt and 5pt data (1296 rows).
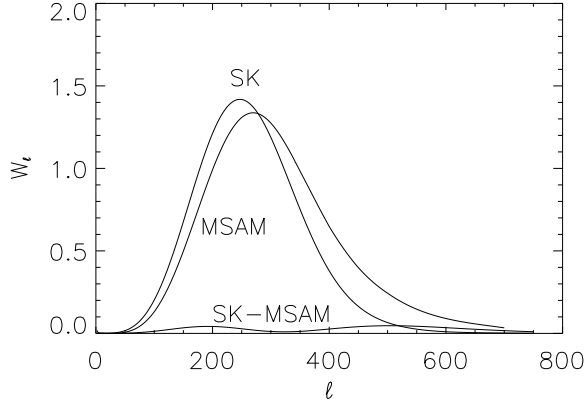
Fig. 5.— The MSAM1-92 and SK95/MSAM Overlap window functions. The window functions are slightly different due to unequal beam size. The window function for the difference is also presented.

sets, their mean and difference. The reduced χ^2 for the sum is 3.43, while the reduced χ^2 for the difference is 1.05, neglecting the anomalous third sample at 14.58 hr in the MSAM1-92 data set. It is clear that both experiments see the same signal on the sky.

To find the consistency of the amplitudes measured by the two experiments, an analysis of Δ as described in Section 10 is performed. The data covariance matrix for the MSAM1-92 data ($C_{D_{MS}}$) is taken to be diagonal, neglecting correlations which were introduced by the removal of offset drifts in the data reduction. For the SK data, $C_{D_{SK}}$ is made from the distribution of the 18 second averages, and includes all known correlations. For analysis of the combined MSAM1-92/SK95 data, the weighted mean is used, and the off diagonal elements on the covariance matrix are generated using

$$C_D^{ij} = C_{D_{SK}}^{ij} \frac{w_{SK}^i w_{MS}^j}{(w_{SK}^j + w_{MS}^i)(w_{SK}^i + w_{MS}^j)} \qquad (31)$$

where w_{SK}^i and w_{MS}^j are the statistical weights of the SK and MSAM1-92 data respectively.

The results of this analysis are presented in Table 8. The errors on Δ include only $\sigma_{\Delta_{sky}}^{inst}$ and do not include sample variance. This is appropriate for comparing the consistency of two measurements of the same sky. The amplitudes are consistent, with SK favoring a higher value than MSAM at the 1σ level.

This analysis has not included calibration uncertainty in the two instruments. For Saskatoon it is
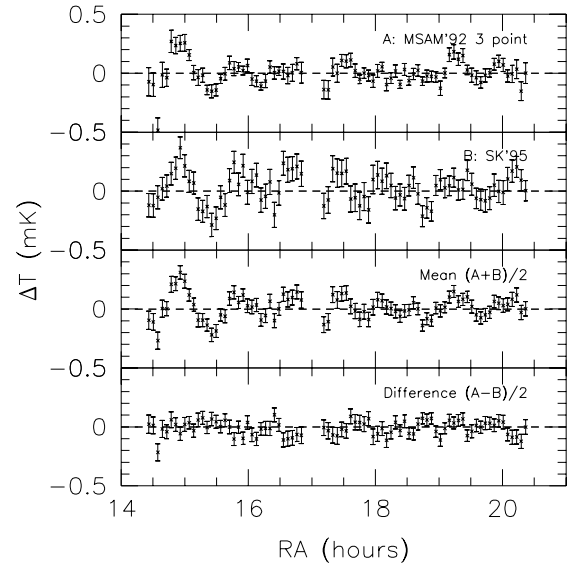

Fig. 6.— MSAM1-92 and SK95/MSAM Overlap compared. The first panel gives the MSAM1-92 3pt data. The second panel gives SK95/MSAM Overlap data for the same region. The third shows the mean and the fourth the difference. The data are in 85 equally spaced RA bins (only 81 have data), and are given in thermodynamic temperature units. The anomalous third bin in the MSAM data set is dropped in the analysis of the comparison. The $0.5°$ FWHM beam spans 0.24 hr of RA.

Table 8
MSAM1-92 and SK compared

	MSAM1-92	SK	Mean	Difference
χ^2/ν	2.66	1.82	3.43	1.05
Δ_{tot}	$88.9\,\mu$K	$104.4\,\mu$K	$76.6\,\mu$K	$52.2\,\mu$K
$\Delta_{inst} \pm \sigma_{\Delta_{inst}}$	$70.5 \pm 5.3\,\mu$K	$79.5 \pm 7.9\,\mu$K	$49.3 \pm 3.9\,\mu$K	$53.2 \pm 4.3\,\mu$K
$\Delta_{sky} \pm \sigma_{\Delta_{inst}}^{inst}$	$53.5 \pm 7.0\,\mu$K	$65.9 \pm 10.2\,\mu$K	$58.6\pm3.3\,\mu$K	$\ldots$
$\delta T_\ell(\Delta_{sky})$	$46.5\,\mu$K	$57.3\,\mu$K	$51\,\mu$K	$\ldots$
δT_ℓ(Full Likelihood)	$52^{+11}_{-6}\,\mu$K	$61^{+19}_{-11}\,\mu$K	$50.9^{+10}_{-6}\,\mu$K	$\ldots$

Note.—A comparison of the MSAM1-92 and SK95/MSAM Overlap data. The reduced χ^2 entries are for the 80 bins in Figure 6, neglecting the anomalous third sample from MSAM1-92. The uncertainties on Δ_{sky} do not include sample variance. The uncertainties on δT_ℓ do. $\delta T_\ell(\Delta_{sky})$ is δT_ℓ inferred from Δ_{sky} using equation (16). Calibration uncertainties are not included.

14%, and for MSAM1-92 it is 10%. Adding these in quadrature yields a relative calibration uncertainty of 17%. A least-squares fit to find the best relative calibration between the two data sets finds $N_{SK}/N_{MSAM} = 0.82 \pm 0.16$. The relative calibration based on the data favors a smaller normalization for SK or a larger normalization for MSAM, but is still consistent with the absolute calibrations used.

The flat band power is found by a full likelihood analysis using the angular spectrum in equation (23). These results are presented in Table 8. The results for the two experiments are fully consistent. Note that calibration uncertainties have not been included in quoted errors.

The original MSAM1-92 analysis is done in terms of the GACF, equation (24). This analysis is repeated here. For MSAM1-92, we find $\sqrt{C(0)} = 70^{+15}_{-9}\,\mu$K , using $\theta_c = 0.92$, which is consistent with the analysis quoted in Cheng et al. (1994). (1994)[4] For SK we find $\sqrt{C(0)} = 81^{+26}_{-15}\,\mu$K . Converted to band power estimates using equation (26) we find $53\,\mu$K and $61\,\mu$K for MSAM1-92 and SK respectively.

A determination of β of the fluctuations yields

$\beta = -0.1 \pm 0.2$. The combination of the SK95 and MSAM1-92 experiments has essentially measured the frequency spectrum of the anisotropy of the fluctuations from $36\,$GHz to $240\,$GHz and have found them to have the frequency spectrum of the CMB. Over this large frequency range no other known source has this spectrum. Free-free emission has $\beta = -1.45$ (as compared to -2.1 in the Rayleigh-Jeans region) and interstellar dust has $\beta = 2.25$ (1.7 in the Rayleigh-Jeans region). The spectral index of these fluctuations is highly inconsistent with these foreground contaminants.

The differences between the two experiments render it very unlikely that the observed signal is the result of mutually common contamination. MSAM is a balloon-borne experiment which observed the sky for several hours, while the Saskatoon experiment is ground based and observed the sky over many days. MSAM is a bolometer based experiment which observes the sky at $180\,$GHz and $240\,$GHz while SK95 is based on $40\,$GHz HEMT amplifiers. MSAM utilizes multi-mode optics while those of the Saskatoon telescope are single mode. MSAM calibrates on Jupiter while SK calibrates on Cas-A. The consistency of the measurements between MSAM and SK indicates that both experiments have measured the anisotropy of the CMB.

---

[4]Cheng et al. (1994) find $50\,\mu$K $< \sqrt{C(0)} < 90\,\mu$K for the 5% to 95% confidence interval. Reanalyzing the MSAM1-92 data, we find $55\,\mu$K $< \sqrt{C(0)} < 99\,\mu$K .
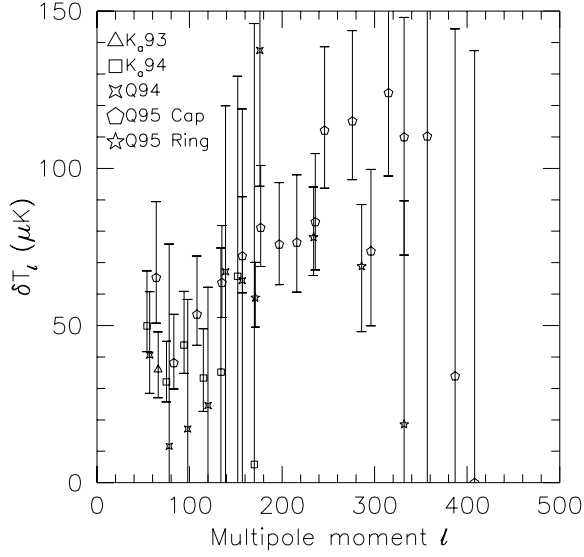
Fig. 7.— The angular spectrum in 37 bins. The results for each synthesized beam for SK93-SK95 is presented separately. These results are given in Table 9. The error bars do not include the $\pm 14\%$ (1σ) overall calibration uncertainty.

13. Determination of The Angular Power Spectrum

The angular spectrum is presented in three ways. The first is to find δT_{ℓ_e} for the data set associated with each of the 37 synthesized beams, H_i, described in Section 9. The results of this are presented in Table 9 and Figure 7. Also included in Table 9 are results from an analysis of Δ as described in Section 10. Note that for SK95 3pt through 10pt, the estimated contribution to the uncertainties due to sample variance, $\sigma_{\delta T_\ell}^{SV}$, is approximately equal to the contribution due to instrument noise, $\sigma_{\delta T_\ell}^{inst}$. Consequently, to significantly reduce the error bars, both better sensitivity and more sky coverage will be required. This representation has significant spatial correlations between entries. For example, the 3pt beams for Q95, Q94 and K_a94 all observe the same sky and at a similar angular scales. It is therefore inappropriate to combine entries simply by taking the weighted mean without taking into account the spatial correlations.

The second way the data are presented is to combine data from spatially correlated synthesized beams between years. To do this, a covariance matrix
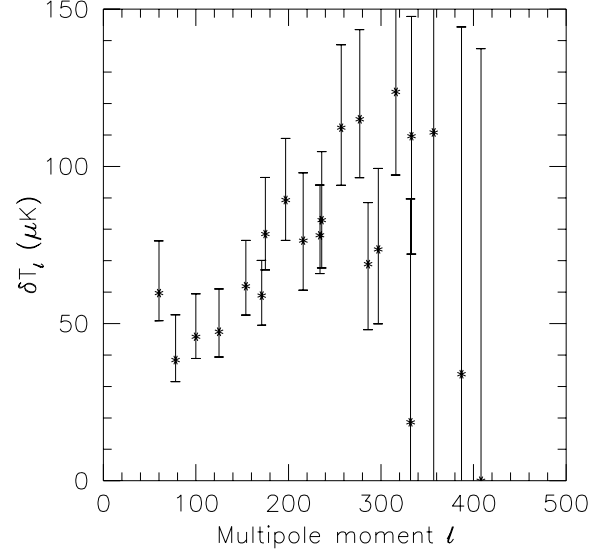

Fig. 8.— The angular spectrum grouped by spatial symmetry. These results are given in Table 10.

		ℓ_e	δT_ℓ
3pt	*Cap*	60	$59^{+17}_{-9}\,\mu K$
4pt		78	38^{+14}_{-7}
5pt		100	46^{+14}_{-7}
6pt		125	47^{+14}_{-8}
7pt		154	62^{+15}_{-9}
3pt	*Ring*	171	59^{+11}_{-9}
8pt	*Cap*	175	79^{+18}_{-11}
9pt		197	89^{+20}_{-13}
10pt		216	76^{+22}_{-16}
4pt	*Ring*	234	78^{+16}_{-12}
11pt	*Cap*	236	83^{+22}_{-15}
12pt		257	112^{+27}_{-18}
13pt		277	115^{+29}_{-19}
14pt		297	74^{+26}_{-24}
5pt	*Ring*	286	69^{+20}_{-21}
15pt	*Cap*	316	124^{+35}_{-26}
16pt		333	110^{+38}_{-38}
17pt		357	$110,\ < 197$
6pt	*Ring*	332	$19,\ < 90$
18pt	*Cap*	382	$88,\ < 191$
19pt		404	$0,\ < 163$

Table 10: The angular spectrum grouped by spatial symmetry. The 14% overall calibration uncertainty is not included in the errors.

TABLE 9

THE ANGULAR SPECTRUM IN 37 BINS

	Bins	Δ_{total}	Δ_{inst}	Δ_{sky}	$\sqrt{I(W)}$	$\delta T_\ell(\Delta_{sky})$	$\sigma^{inst}_{\delta T_\ell}$	$\sigma^{SV}_{\delta T_\ell}$	ℓ_e	δT_ℓ
K_a93 3pt	24	$49\,\mu K$	$37\,\mu K$	$32\,\mu K$	1.04	$31\,\mu K$	$5\,\mu K$	$11\,\mu K$	66^{+28}_{-19}	$36^{+12}_{-9}\,\mu K$
K_a94 3pt	24	65	44	49	1.16	42	4	12	56^{+21}_{-18}	50^{+18}_{-8}
4pt	24	48	42	24	0.88	27	9	11	76^{+21}_{-19}	32^{+13}_{-6}
5pt	24	42	33	26	0.73	36	10	10	96^{+21}_{-19}	44^{+17}_{-9}
6pt	48	65	56	33	0.62	54	12	9	115^{+21}_{-19}	33^{+16}_{-11}
7pt	48	81	75	30	0.54	56	27	13	134^{+22}_{-19}	$35, \ < 75$
8pt	48	111	101	47	0.48	47	36	12	152^{+23}_{-18}	$66, \ < 129$
9pt	48	127	146	0	0.43	0	$\ldots$	12	170^{+24}_{-17}	$6, \ < 146$
Q94 3pt	24	86	73	45	1.22	47	10	11	59^{+18}_{-21}	41^{+20}_{-12}
4pt	24	83	65	53	0.93	57	9	10	81^{+16}_{-24}	$12, \ < 76$
5pt	24	59	55	22	0.77	28	19	10	100^{+17}_{-23}	$17, \ < 58$
6pt	48	75	82	0	0.67	0	$\ldots$	9	120^{+17}_{-24}	$25, \ < 62$
7pt	48	109	99	45	0.59	77	27	12	139^{+18}_{-24}	$67, \ < 120$
8pt	48	112	107	32	0.53	61	50	11	157^{+19}_{-23}	$64, \ < 119$
9pt	48	136	129	44	0.48	91	58	11	176^{+20}_{-23}	138^{+59}_{-43}
Q95 *Cap* 3pt	24	101	78	63	1.29	49	8	11	64^{+12}_{-27}	65^{+24}_{-14}
4pt	24	65	56	33	1.02	32	11	10	83^{+13}_{-29}	38^{+16}_{-8}
5pt	24	62	43	44	0.81	55	6	9	108^{+8}_{-32}	54^{+19}_{-10}
6pt	48	76	58	49	0.76	64	8	8	135^{+6}_{-37}	64^{+18}_{-11}
7pt	48	74	53	52	0.67	78	7	10	158^{+7}_{-38}	72^{+19}_{-12}
8pt	48	76	58	50	0.59	84	9	10	178^{+6}_{-38}	81^{+20}_{-12}
9pt	48	69	54	43	0.54	79	10	9	197^{+8}_{-37}	76^{+20}_{-13}
10pt	48	70	60	37	0.50	74	16	11	217^{+6}_{-38}	76^{+22}_{-16}
11pt	48	63	56	31	0.46	66	18	11	237^{+8}_{-37}	83^{+22}_{-15}
12pt	48	80	60	53	0.42	126	13	11	257^{+8}_{-36}	112^{+27}_{-18}
13pt	48	78	59	51	0.40	127	14	11	277^{+10}_{-35}	115^{+29}_{-19}
14pt	48	74	64	38	0.37	102	24	11	297^{+10}_{-34}	74^{+26}_{-24}
15pt	48	78	73	28	0.35	79	48	10	316^{+11}_{-34}	124^{+35}_{-26}
16pt	48	96	73	63	0.33	190	22	8	333^{+13}_{-31}	110^{+38}_{-38}
17pt	48	95	78	53	0.31	172	30	8	357^{+13}_{-31}	$110, \ < 197$
18pt	48	97	84	48	0.29	166	41	8	382^{+12}_{-30}	$88, \ < 191$
19pt	48	99	91	40	0.27	150	63	8	404^{+13}_{-29}	$0, \ < 163$
Q95 *Ring* 3pt	96	107	77	74	1.14	65	5	7	170^{+66}_{-54}	59^{+11}_{-9}
4pt	96	104	78	68	0.85	80	8	9	234^{+67}_{-52}	78^{+16}_{-12}
5pt	96	101	89	48	0.70	69	18	8	286^{+79}_{-39}	69^{+20}_{-21}
6pt	96	106	107	0	0.59	0	$\ldots$	8	332^{+99}_{-16}	$19, \ < 90$

NOTE.— Results from each synthesized beam from SK93, SK94 and SK95. The SK93 entries are from Netterfield et al. (1995). The K_a94 and Q94 entries differ slightly from those found in Netterfield (1994) due to the inclusion of East to West correlations in the analysis. Δ_{total} is the raw rms of the binned data. Δ_{inst} is the rms predicted by the data covariance matrix, C_D. $\Delta^2_{sky} = \Delta^2_{total} - \Delta^2_{inst}$ gives the sky rms. $\delta T_\ell(\Delta_{sky})$ gives the band power inferred from Δ_{sky} using equation (16). $\sigma^{inst}_{\delta T_\ell}$ estimates the contribution to the error bars due to the instrument noise and $\sigma^{SV}_{\delta T_\ell}$ estimates the contribution to the error bar due to sample variance. The limits on ℓ_e are for where the window function falls to $e^{-1/2}$ of the peak value. The final column lists δT_ℓ from the full likelihood analysis. The overall 14% calibration uncertainty is not included in the errors.

ℓ_e	δT_ℓ (μK) Low Cut	δT_ℓ (μK) High Cut	δT_ℓ (μK) Definitive	m
87^{+39}_{-29}	47^{+8}_{-5}	...	49^{+8}_{-5}	$-0.8^{+1.2}_{-0.1}$
166^{+30}_{-43}	72^{+8}_{-7}	...	69^{+7}_{-6}	$0.5^{+0.4}_{-0.4}$
237^{+29}_{-41}	102^{+11}_{-11}	87^{+9}_{-8}	85^{+10}_{-8}	$-0.4^{+0.5}_{-0.2}$
286^{+24}_{-38}	102^{+12}_{-15}	83^{+10}_{-9}	86^{+12}_{-10}	$-0.5^{+0.7}_{-0.2}$
349^{+44}_{-41}	93^{+23}_{-32}	60^{+15}_{-22}	69^{+19}_{-28}	...

Table 11: The angular spectrum in 5 bins. The first bin is comprised of the 3pt to 6pt *Cap* data from all three years. The second is from the 7pt to 9pt *Cap* data and the 3pt *Ring* data. The third is 10pt to 12pt *Cap* and 4pt *Ring* . The fourth is 13pt to 15pt *Cap* and 5pt *Ring* . The fifth is 16pt to 19pt *Cap* and 6pt *Ring* . See Section 4 for a description of the cut levels. m is the angular spectral index within each bin.

$C_D + C_T$ is made which includes all of the data corresponding to a given spatial symmetry. For example, the K_a94, Q94 and Q95 3pt data forms a 144×144 matrix. The band power is then evaluated using a maximum likelihood test. An effective window function is generated using equation (22). The K_a93 3pt data has largest spatial overlap with the 94/95 4pt data and is included there. These results are presented in Table 10 and Figure 8. The tendency for a rising spectrum is evident here though the scatter in the points, particularly at high ℓ, is still considerable.

Finally, the data are combined into 5 angular scale bins and presented in Table 11 and Figure 9. To produce each of these bins, all of the data which is sensitive to a given range of angular scales is combined using the full correlation matrix (see Section 7). For instance, the first bin is comprised of the 3pt to 6pt *Cap* data from all three years. The effective window functions for each bin using equation (22) are presented in Figure 10.

Also presented in Table 11 are values for the angular spectral index m (see Section 9). The negative spectral index around $\ell \approx 80$ which was reported in Netterfield (1994) with the 1994 data alone is again seen in the lowest angular bin. The lowest four points in Figure 8 also shows this locally falling spectrum. However, this trend is dominated by the 3pt data being high. Additionally, for each of the 5 angular bins, including the first one, the slope is consistent with 0. The angular spectrum of the whole sky may have a dip at these scales, or this effect could be a result of
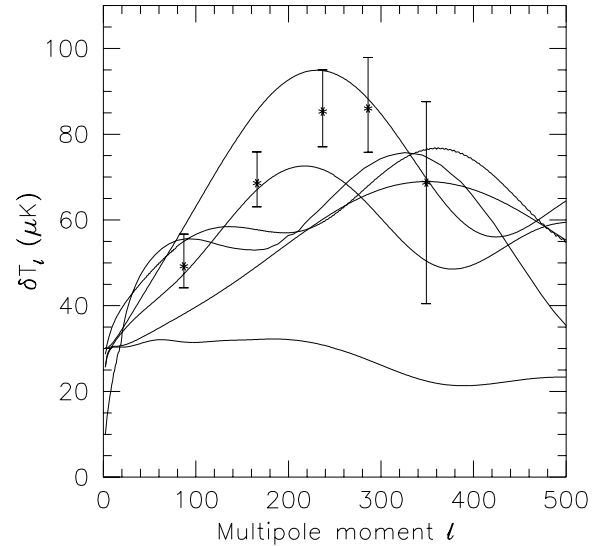

Fig. 9.— The angular spectrum in 5 bins. The results are tabulated in Table 11 and the effective window functions are shown in Figure 10. Predicted spectra from six representative theories are also shown. They are, from top to bottom at $\ell = 160$ a flat Λ+CDM Model with $\Omega_\Lambda = 0.7$ (Ratra and Sugiyama 1995), Standard CDM (Ratra et al. 1995), a Texture model (Crittenden and Turok, 1995) a PPI model (Peebles, 1995) an $\Omega = 0.4$ open model (Ratra et al. 1995), and a model with reionization (Sugiyama 1995). The texture model is arbitrarily normalized. All others are normalized to COBE. To accurately compare each of these spectra with the data, they must be convolved with the window functions in Figure 10. The 14% overall calibration uncertainty is not included in the error bars. This effects the normalization of the spectrum, but not the shape.
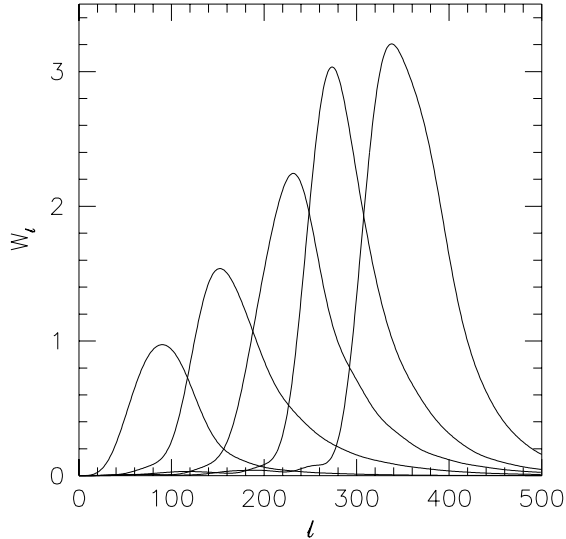
Fig. 10.— The 5 bin effective window functions. These have been generated from the window functions of the contributing effective antenna patterns using equation (22).

sample variance. This issue will be resolved by extended sky coverage to reduce sample variance.

While all known correlations have been taken into account in generating the likelihoods for each of the combined groups, there are still some correlations between groups. They are small (< 0.2), however, and may be ignored for most analysis.

Not included in the quoted error bars are the effects of calibration and beam uncertainties. As discussed, the calibration uncertainty is 14% (1σ), mainly due to uncertainty in the temperature scale of Cas-A. This has very little effect on the uncertainty of the spectral index, β, and no effect on the shape of the angular spectrum. Rather this has only an effect on the over-all temperature scale. This large normalization uncertainty must be included in any comparison with theoretical predictions.

Beam uncertainties, as well as contributing to calibration errors, also produce uncertainties in the angular spectrum. For uncertainties in the beamwidth along the elevation axis, the only effect is in the calibration (miss-estimating the beam solid angle in predicting the signal from Cas-A), and has been included in that error bar. For uncertainties in the azimuth beam width the effect is a function of the weight-

ing vectors used. For the 4pt synthesis, where the physical beam width is small compared to the width of the synthesized lobes, only the temperature scale is effected, as with the elevation beam. For the 13pt synthesis, however, the additional effect of mis-stating the beam overlap between points very nearly cancels the effect on the calibration. The result of this is that the 2% azimuth beam uncertainty yields an additional 2% relative uncertainty between the 4pt and 13pt synthesized beam data. This effect is small for this experiment given the error bars on the spectrum and is ignored.

14. Foreground Contamination

The angular spectra presented in the previous section are for the microwave sky at 40 GHz. There are, however, potential sources of foreground contamination. Two major classes are diffuse Galactic emission, and unresolved point sources. Limits may be placed on the level of both of these potential contaminants.

Potential sources of diffuse Galactic contamination include dust, synchrotron, and free-free emission. The level of dust contamination at 40 GHz and $\ell = 100$ has be estimated to be less than $2\,\mu K$ (Tegmark & Efstathiou 1995), which is far smaller than the signals measured here. Similarly, recent measurements of the amplitude of diffuse free-free emission based on H_α emission have been made for the Saskatoon observing region (Gaustad et al. 1995; Simonetti et al. 1995). These measurements place an upper limit of $6\,\mu K$ at 30 GHz for the SK93 3pt beam. Once again this is too small to account for the observed signals. An analysis of high latitude Galactic emission in the COBE 2 year data places similar limits on both foregrounds at large angular scales (Kogut et al. 1995). An estimate of the amplitude of synchrotron emission can be made by extrapolating radio maps at 408 MHz (Haslam, C.G.T. et al. 1982) and 1.4 GHz (Reich & Reich 1986) to 30 GHz assuming a temperature spectral index of $\beta = -2.8$. This predicts a signal of less than $5\,\mu K$ in K_a93, which is much smaller than the measured signals. However, if the spectral index of the synchrotron emission varies spatially by $\delta\beta \approx 0.05$, then $30\,\mu K$ signals could be expected. The spectral index of these fluctuations would still be characterized by $\beta \approx -2.8$.

The most powerful discriminant against foreground contamination is based on the frequency spectrum of

TABLE 12
Bright Point Sources

Source	ν_o	Flux at ν_o	Spectral Index α	Flux at 40 GHz	Reference
0014+81	10.7 GHz	0.73 Jy	0.36	1.2 Jy	S5
0210+860 (3C61.1)	30.0	1.0	0.2	1.1	HR
0454+844	10.0	1.5	0.0	1.5	K
0615+820	10.7	0.86	0.0	0.86	E,K
0740+82	10.7	0.65	-0.47	0.35	HR, S5
1003+83	10.7	0.66	-0.10	0.58	S5
1039+811	90.0	0.80	0.0	0.80	IRAMc
1053+815	20.0	0.4	0.43	0.54	E,VLBIc
1050+812	10.7	1.1	-0.1	0.96	K
1221+809	10.7	0.6	+0.2	0.78	S5, VLAc
1637+8239 (NGC6251)	10.7	0.8	-0.4	0.47	HR
1637+826	10.7	0.73	-0.4	0.43	S5,VLAc
2342+821	30.0	0.8	0.2	0.85	HR, S5

NOTE.— Listed are parameters for the brightest point sources used in the estimate of the level of point source contamination. The flux at 40 GHz is extrapolated from the measurement at ν_o by $S(\nu) = S(\nu_o)(\nu/\nu_o)^\alpha$, where $\alpha = \beta + 2$. The measured value from the literature for α used where possible. Otherwise $\alpha = 0$ (flat spectrum or constant flux with frequency) is assumed. The data are obtained from Eckart et al. 1986 (E), Herbig & Readhead 1992 (HR), Steppe et al. 1992 (IRAMc), Kühr et al. 1981a (K), Kühr et al. 1981b (S5), Perley 1982 (VLAc) and Edelson 1987 (E).
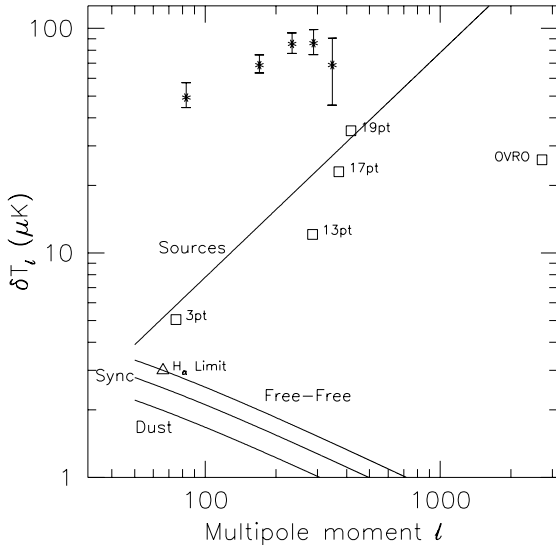
Fig. 11.— Estimated levels of foreground contamination at 40 GHz. The 5 bin data from this experiment are given as asterisks. The estimated angular spectra for the various foreground sources are from Tegmark and Efstathiou (1995). The free-free angular spectrum has been renormalized for our observing region using a limit based on H_α emission (Gaustad et al. 1995; Simonetti et al. 1995). An upper limit for the normalization of the synchrotron spectrum has been estimated by extrapolating the 408 MHz Haslam map to 40 GHz for our observing region (Haslam et al. 1982, Wollack et al. 1993). The square boxes represent contributions to our data estimated by extrapolating exiting point source surveys to 40 GHz (see text). Also indicated is an upper limit on sources at smaller scales based on the OVRO Ring experiment (Meyers, Readhead, and Lawrence, 1993) extrapolated from 20 GHz.

the fluctuations (β). In Section 11, for $\ell \approx 73$, β was found to be 0.2 ± 0.3 which is inconsistent with the spectral index of dust ($\beta = 1.7$), free-free emission ($\beta = -2.1$), or synchrotron emission ($\beta = -2.8$). Additionally, since the angular spectrum for galactic emission falls as $\delta T_\ell \propto \ell^{-1/2}$ (Tegmark & Efstathiou 1995), it is very unlikely that the galaxy is a significant contaminant at any angular scale.

Of more concern for several reasons is potential contamination by unresolved point sources. Firstly, the angular spectrum of a family of point sources is expected to rise as $\delta T_\ell \propto \ell$, so the β limits placed at large angular scales are weaker at smaller angular scales. Additionally, since the mechanism for radiation varies between individual sources, the expected β also varies, and in many cases is not accurately described by a simple power law. This is of particular concern since no flux-limited survey of the SK observing region in has been performed over our frequencies (26 GHz to 40 GHz). However, it is still possible to make some estimates of the level of contamination via comparison with MSAM1-92, source counts from the OVRO Ring experiment (Meyers, Readhead, & Lawrence 1993) at smaller scales and an extrapolation of existing point source surveys.

While β varies from source to source, it is expected that over a sufficiently wide frequency range no foreground source will have a spectrum consistent with $\beta = 0$. Consequently our comparison of SK95 with MSAM1-92 which yields a limit on β of 0.1 ± 0.2 with a frequency baseline from 40 GHz to 240 GHz assures that the sky covered by both experiments is devoid of significant point contamination. However, this field only represents 8 square degrees of the total of 200 square degrees observed by SK95.

A second approach is to use results from other experiments and point source surveys. The OVRO Ring experiment has observed 96 fields at 20 GHz. They find $\delta T_\ell = 103 \, \mu$K at $\ell_e = 2017$. Here we make the assumption that the signal is dominated by Poisson distributed unresolved point sources. Extrapolating in angular scale by $\delta T_\ell \propto \ell$ to $\ell = 404$, the angular scale of the 19pt data set, one arrives at an expected contribution of $21 \, \mu$K. Since OVRO Ring was performed at 20 GHz, this number needs to also be scaled in frequency. A conservative estimate of the 'typical' β for a point source is that its flux is constant in frequency, (i.e.,flat spectrum or $\beta = -2$). Thus, an estimate of the point source contribution at the smallest scales of the SK experiment based on OVRO Ring

source counts is $10\,\mu$K at 40 GHz.

As a final estimate of the level of point source contamination, the expected amplitude of known point sources in the observing region is extrapolated. Table 12 lists the brightest of these. In addition to the sources listed in Table 12, all of the sources in the S5 catalog (Kühr et al. 1981b) are used. Based on an analysis of IRAS faint sources, it is considered unlikely that a new population of sources exists within our observing frequencies (Condon et al. 1995). The spectral index from the literature is used to extrapolate to 40 GHz whenever possible. If a measured frequency spectral index is not known, the source is assumed to be of constant flux with frequency. A source map of the observing area is made, and the SK observing strategy simulated on it. The largest estimated contribution is to the 19pt data, and is $\delta T_\ell = 35\,\mu$K , which could be significant. However, from Table 9, the 19pt data yields a $163\,\mu$K upper limit with a maximum likelihood at $0\,\mu$K . The estimated contribution to the 17pt data is $23\,\mu$K , which would imply a 4% contribution to our $69\,\mu$K detection at these scales. The predicted signal is dominated by sources in RA bins 5 and 10. The measured 17pt data show no excess in these bins, and re-analyzing the data with these bins deleted changes the most likely value for the 17pt data by less than 1%. For the 13pt data, at $\ell = 277$, the expected contribution is $\delta T_\ell = 12\,\mu$K . From Table 9, the measured value is $115\,\mu$K . Subtracting the source contribution in quadrature yields less than a 1% effect.

The data, along with estimated contributions from foreground contaminants are presented in Figure 11. The indications are that the SK data are not seriously contaminated by foreground sources. However, extending the coverage to smaller angular scales will require improved discrimination from point sources.

15. Discussion

The rich set of internal and external consistency checks inherent to this experiment indicate that a signal fixed to the celestial sphere has been detected. The limits placed on the frequency spectral index β rule out significant contamination from diffuse Galactic emission. The limits on β over a very large frequency range placed by the successful comparison with the MSAM1-92 experiment further reduce the likelihood of significant contribution to the signal by foreground contaminants. Conservative extrapola-

tions from existing point source catalogs strengthen this argument. The evidence is compelling that the signal which has been detected is due to anisotropies in the CMB.

This experiment has measured the angular spectrum of these anisotropies simultaneously with one experiment and with equal calibration error at all angular scales. We find that the spectrum rises from $\delta T_\ell = 49^{+8}_{-5}\,\mu$K at $\ell = 87$ to $85^{+10}_{-8}\,\mu$K at $\ell = 237$. This can be used to place significant limits on the reionization history of the universe, and, within a given theoretical framework, begin to place limits on cosmological parameters. A quantitative comparison with theory will presented elsewhere.

Given the relative complexity of this analysis, it is important to mention that much of the analysis has been repeated with completely different programs by two of the authors to verify accuracy. The consistency of the naive Δ based tests with the full likelihood analysis further strengthens our confidence in our programs and techniques. In addition, Andrew Jaffe and J.R. Bond at CITA have repeated and extended our analysis of the SK93 and SK94 data, again confirming our analysis.

To improve the discriminating power of this experiment several things are needed besides reducing the size of the error bars. First of all, it must be confirmed at high ℓ. Additionally, a wider frequency coverage at smaller scales will improve discrimination against point sources. A better calibration will improve comparison with COBE, effectively increasing the range of angular scales over which a theory can be tested. It is possible to make a map of the CMB anisotropy from these data. A map of an extended region of the sky with better signal to noise will be useful to distinguish between Gaussian and non-Gaussian models.

REFERENCES

Bennet, C. L. et al. 1992, ApJ, 396, L7

Bond, J. R. 1995, Astrophys Lett & Comm, 2

Bond, J. R., Crittenden, R., Davis, R. L., Efstathiou, G. & Steinhardt, P. J. 1994, Phys. Rev. Lett., 72, 1

Bond, J.R. 1995, "Theory and Observations of the Cosmic Background Radiation" in Cosmology and the Large Scale Structure, ed. R. Schaeffer, Elsevier Netherlands. Proc. Les Houches School, Session LX, Aug., 1993

Cheng, J. R. et al. 1994, ApJ, 422, L37

Condon, J. J., Anderson, E., & Broderick, J. J. 1995 AJ, 109, 2318

Crittenden, R. G. & Turok, N. 1995, Phys. Rev. Lett., 75, 14

De Benardis, P. et al. 1994, ApJ, 422, 33

Devlin, M. J. et al. 1994, ApJ, 430, 1

Dragovan, M., Ruhl, J. E., Novak, G., Platt, S. R., Crone, B., Pernic, R. & Peterson, J. B. 1994, ApJ, 427, 67

Eckart, A., Witzel, A., Biermann, P., Johnston, K. J. & Simon, R. 1986, A&A, 168, 17

Edelson, R. A. 1987, AJ, 94, 1150 (VLBI Calibrators)

Ganga, K. M., Cheng, E., Meyer, S., & Page, L. 1993, ApJ, 410, L57

Gaustad, J. E., Oh, E. S., McCullough, P. R. & Van Buren, D. 1995, BAAS, 27, 823

Gundersen, J. O. et al. 1995, ApJ, 443, 57

Gutierrez De La Cruz, C. M. et al. 1995, ApJ, 442, 10

Haslam, C. G. T., Salter, C. J., Stoffel, H., & Wilson, W. E. 1982, A&AS, 47, 1

Herbig, T. & Readhead, A. 1992, ApJS, 81, 83

Kamionkowski, M., Spergel, D. N., & Sugiyama, N. 1994, ApJ, 426, L57

Jarosik, N. 1996, IEEE Trans on MTT, 44, 2

Jungman, G., Kamionkowski, M., Kosowsky, A., & Spergel, D. N. 1995, Astro-Ph Preprint/9507080

Knox, L. 1995, CITA, Private Communication

Kogut, A. et al. 1995, ApJ, in press

Kühr, H., Witzel, A., Pauliny-Toth, I. I. K. & Nauber, U. 1981, Astr. Ap. Suppl. Ser, 45, 367

Kühr, H., Pauliny-Toth, I. I. K., Witzel, A., Schmidt, J. 1981, AJ, 86, 854 (The S5 survey)

Meyers, S. T., Readhead, A. C. S. & Lawrence, C. R. 1993, ApJ, 405, 8

Netterfield, C. B. 1995, Ph.D. Thesis, Princeton University

Netterfield, C. B., Jarosik, N. C., Page, L. A., Wilkinson, D., & Wollack, E. J. 1995, ApJ, 455, L69

Page, L. A. et al. 1994 in Proc. CWRU Conf. on the CMB, CMB Anisotropies Two Years After COBE: Observations, Theory, and the Future, ed. L. Krauss (Sigapore: World Scientific)

Peebles, P. J. E. 1994, ApJ, 419, L49

Peebles, P. J. E. 1995, Private Communication

Perley, R. 1982, AJ, 87, 859 (VLA Calibrators)

Ratra, B. & Sugiyama, N. 1995, submitted

Ratra, B. Banday, A. J., Górski, K. M., & Sugiyama, N. 1995, submitted

Readhead, A. C. S., Lawrence, C. R., Meyers, S. T., Sargent, W. L. W., Hardebeck, H. E. & Moffet, A. T. 1989, ApJ, 346, 566

Reich, P. & Reich, W. 1986, A&AS, 63, 205

Simonetti, J. H., Dennison, B. & Topasna, G. A. 1995, ApJ, in press

Smoot, G. F. et al. 1992, ApJ, 396, L1

Steppe, H., Liechti, S., Mauersberger, R., Koempe, C., Brunswig, W. & Ruiz-Moreno, M. 1992, Astr. Ap. Suppl. Ser, 96, 441 (IRAM Pointing Calibration List)

Sugiyama, N. 1995, ApJS, 100, 281

Tegmark, M. & Efstathiou, G. 1995, MNRAS, submitted

Tucker, G. S., Griffin, G. S., Nguyen, H. T., Peterson, J. B. 1993, ApJ, 419, L45

White, M. & Scott, D. 1994, in Proc. CWRU Conf. on the CMB, CMB Anisotropies Two Years After COBE: Observations, Theory, and the Future, ed. L. Krauss (Sigapore: World Scientific)

White, M., Scott, D. & Silk, J. 1994, ARA&A, 319

Wollack, E. J., Jarosik, N. C., Netterfield, C. B., Page, L. A. & Wilkinson, D. 1993, ApJ, 419, L49

Wollack, E. J. 1994, Ph.D. Thesis, Princeton University

Wollack, E. J., Jarosik, N. C., Netterfield, C. B., Page, L. A. & Wilkinson, D. 1994, Astrophys. Lett. & Comm., 35, 217

Wollack, E. J., Devlin, M. J., Jarosik, N. C., Netterfield, C. B., Page, L. A. & Wilkinson, D. 1996, ApJ, submitted